Crystallization and Magnetic Property of FeCoZrB Alloy

Yaming Sun[a,*], Lihua Liu[a],
Yanxiang Sun[b] and Xingwang Liu[a]

[a] *College of Physics, Jilin Normal University, Haifeng Street 1301, 136000 Siping, China*
[b] *Chengxi Power Supply Company, State Grid Tianjin Electric Power Company, Hongqi Road 278, 300190 Tianjin, China*

Received: 08.09.2025 & Accepted: 07.11.2025

Doi: 10.12693/APhysPolA.148.313 *e-mail: sunyaming@jlnu.edu.cn

Samples of the nanocrystalline soft magnetic alloy $Fe_{42}Co_{42}Zr_7B_9$ were prepared by annealing the as-quenched amorphous precursors at various temperatures to investigate the crystallization behavior of the samples and the evolution of their magnetic properties. Differential scanning calorimetry revealed two distinct stages, namely (i) the primary crystallization of the α-Fe solid solution and (ii) the formation of $ZrCo_3B_2$ and Fe_3Zr phases. Grain growth proceeded gradually in the early stage and increased rapidly in the later stage of crystallization. The lattice constant initially increased and then decreased at about 600°C due to the incorporation of Zr into the α-Fe lattice. The specific saturation magnetization (M_s) and coercivity (H_c) followed similar two-stage trends, i.e., M_s first increased and then decreased, while H_c slightly increased below 600°C and rose sharply thereafter due to grain growth and phase transformations. Thus, precise control of the annealing temperature in FeCoZrB alloys allows for tuning of the microstructural and magnetic properties, offering pathways toward high-efficiency, soft magnetic components.

topics: nanocrystalline alloy, crystallization process, lattice constant, coercivity

1. Introduction

The remarkable properties of Fe-based nanocrystalline soft magnetic alloys can be attributed to their two-phase structure, in which body-centered cubic (bcc) Fe crystallites (10–20 nm) are embedded within an amorphous ferromagnetic matrix [1]. When fine ferromagnetic nanocrystals are exchangeably coupled through the surrounding amorphous phase, the magnetocrystalline anisotropy is effectively averaged over numerous grains, resulting in superior soft magnetic performance [2].

By partially substituting Fe with Co, FeCo-based nanocrystalline soft magnetic alloys exhibit higher Curie temperatures and saturation magnetizations than their Co-free counterparts [3]. These enhancements make them suitable for high-temperature applications. They represent a critical class of soft magnetic materials with a wide range of technological applications and have been widely investigated [4–9]. A typical representative of this family is the HITPERM series alloy [FeCoMB(Cu) (M = Nb, Zr, Hf)] [10]. Elements such as Zr and Nb are generally assumed to be distributed in the remaining amorphous material, where they play a role in inhibiting grain growth.

Heat treatment plays a key role in enhancing material performance by modifying the microstructure [11]. It is essential for processing many types of alloy materials [12–15]. Fe-based nanocrystalline soft magnetic alloys are commonly fabricated via partial crystallization of an amorphous precursor. Heat treatment temperature directly affects atomic diffusion and phase precipitation, which in turn influences the grain number, grain size, crystallization volume fraction, and the composition of precipitated phases during alloy crystallization [1].

In this study, samples of amorphous $Fe_{42}Co_{42}Zr_7B_9$ alloy were prepared and annealed at various heat treatment temperatures. The crystallization behavior and magnetic properties were analyzed, and the thermal evolution was divided into two stages. Notably, in the mid-crystallization stage the Zr element is not completely distributed in the remaining amorphous matrix but partially dissolves into the lattice.

2. Experiments

An ingot of nominal compositionthe made of an alloy of $Fe_{42}Co_{42}Zr_7B_9$ was prepared by arc melting high-purity Fe (99.98 mass%), Co (99.95 mass%),

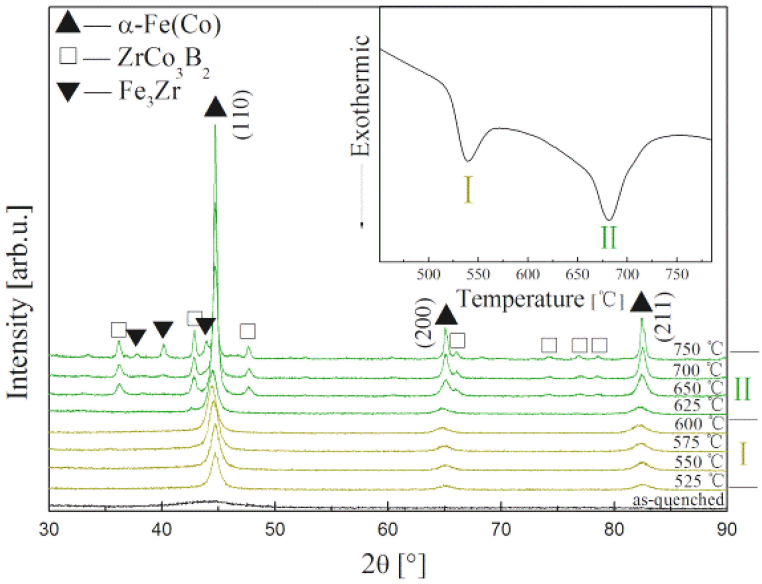

Fig. 1. XRD patterns of $Fe_{42}Co_{42}Zr_7B_9$ alloy in the as-quenched and annealed states. The inset shows the DSC trace of the as-quenched sample.

Zr (99.92 mass%), and B (99.999 mass%) under a Ti-gettered argon atmosphere. During the melting process, the ingot was rotated and magnetically stirred to ensure compositional homogeneity. Melt-spun ribbons (approximately 10 mm wide and 40 μm thick) were fabricated by inductively melting the alloy and ejecting the melt onto a copper wheel rotating at 38 m/s under pressurized argon. The amorphous ribbons were then isothermally annealed in a vacuum tube furnace for 40 min to obtain nanocrystalline alloys.

Differential scanning calorimetry (DSC) data were collected using a simultaneous thermal analyzer (STA 449F5). X-ray diffraction (XRD) patterns were recorded using a D/Max-2500/PC diffractometer (Cu K_α, $\lambda = 1.5406$ Å, step of 0.02°, scan rate = 4°/min). The lattice constant and grain size of α-Fe(Co) were calculated using Jade 5.0. Transmission electron microscopy (TEM, FEI Talos F200X, 200 kV) and scanning transmission electron microscopy with energy dispersive spectroscopy (STEM–EDS) were used to characterize the sample morphology and elemental distribution. Magnetic hysteresis loops were measured using a Dynacool-9T physical property measurement system (PPMS).

3. Results and discussion

Figure 1 presents the XRD patterns of the $Fe_{42}Co_{42}Zr_7B_9$ alloy in both the as-quenched and annealed states. The as-quenched sample exhibited a broad diffuse diffraction halo with no sharp peaks, confirming its amorphous structure. The inset depicts the DSC trace of the as-quenched alloy; two exothermic peaks are evident, indicating a two-stage crystallization process. Based on the DSC curve, the annealing process is divided into two temperature ranges (inset of Fig. 1).

After annealing at 525°C, Bragg reflections corresponding to the (110), (200), and (211) planes of the α-Fe(Co) phase appeared, indicating the precipitation of a single bcc α-Fe(Co) crystalline phase from the amorphous matrix. When the annealing temperature exceeded 625°C, the $ZrCo_3B_2$ phase formed in addition to α-Fe(Co). At 750°C, both $ZrCo_3B_2$ and Fe_3Zr phases were observed.

With increasing annealing temperature, the full width at half maximum of the (110) diffraction peak narrowed, and the peak position shifted first toward lower angles and then toward higher angles. These changes suggest an increase in the grain size and a variation in the lattice constant of the crystalline phase.

The grain size (D [nm]) and lattice constant (a [Å]) of the α-Fe(Co) phase as functions of the annealing temperature (T_a) are presented in Fig. 2a and 2b, respectively. Both parameters exhibited noticeable changes during nanocrystallization as the annealing temperature increased.

In the early stage of crystallization, grain growth was slow, because Zr atoms were distributed in residual phases, which suppressed grain growth. However, in the later stage, the grain size increased rapidly due to the precipitation of a large amount of Zr-containing compounds.

The lattice constants of pure α-Fe and α-FeCo were 2.8664 and 2.8550 Å, respectively. At 525 and 550°C, the measured lattice constants were lower than those of pure Fe but higher than those of pure α-FeCo, indicating slight dissolution of Co

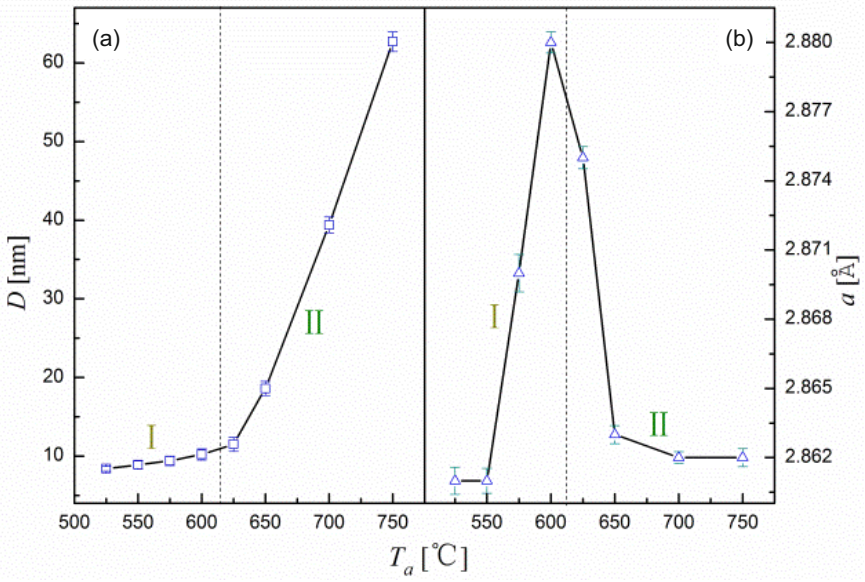

Fig. 2. Variation of (a) grain size and (b) lattice constant of the α-Fe(Co) phase with annealing temperature (T_a).

in α-Fe. Furthermore, the lattice constant increased rapidly, reaching a maximum at 600°C, which exceeded the value for pure Fe. This indicates incorporation of large-radius Zr atoms into the α-Fe lattice. At this temperature, the solid solubility of Zr appeared to reach saturation. During the early stage of crystallization of Zr-containing Fe-based alloys, Zr is distributed in the residual amorphous phase. However, we observed partial dissolution of Zr into the lattice. Upon further increase in temperature, this Zr combined with Co and B to form the $ZrCo_3B_2$ phase, thereby reducing the Zr content in α-Fe. Above 600°C, the lattice constant rapidly decreased and then stabilized between those of pure Fe and α-FeCo, again suggesting partial Co dissolution in α-Fe at elevated temperatures.

Based on the previously described observations, the two peaks in the DSC curve correspond to (i) the primary crystallization of the α-Fe solid solution and (ii) the formation of $ZrCo_3B_2$ and Fe_3Zr phases.

Figure 3 shows the high-resolution TEM (HRTEM) image and the corresponding fast Fourier transform (FFT) pattern of the sample annealed at 550°C. FFT analysis confirmed that the α-Fe(Co) phase grains were oriented along the [111] crystallographic direction.

Bright-field (BF) and high-angle annular dark field (HAADF) TEM images and elemental maps of the $Fe_{42}Co_{42}Zr_7B_9$ alloy annealed at 550°C, shown in Fig. 4, provide further information on the elemental distributions within the alloy. The TEM image revealed a small number of nanocrystals. The Fe-rich regions corresponded to the primary bcc α-Fe(Co) crystals, while the remaining Fe was distributed within the residual amorphous matrix. No apparent difference in Co concentration was

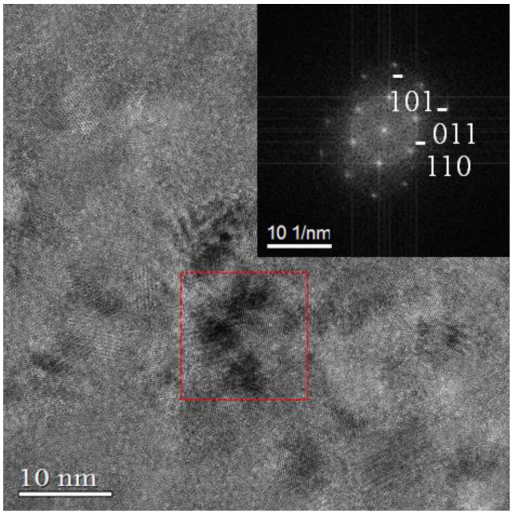

Fig. 3. HRTEM image and the FFT pattern corresponding to the red box (inset) of the alloy annealed at 550°C.

observed between the nanocrystals and the amorphous matrix. Zr was predominantly located in the residual amorphous phase. These results indicate that annealing at 550°C produces a two-phase structure, wherein bcc α-Fe(Co) crystals are embedded within the amorphous matrix.

Figure 5 shows the variation of coercivity (H_c) and specific saturation magnetization (M_s) of the $Fe_{42}Co_{42}Zr_7B_9$ alloy as a function of annealing temperature (T_a). The overall trend can be divided into two stages. In the first stage (below 600°C), H_c remained low and stable, partly due to stress relaxation in the amorphous ribbons during heat

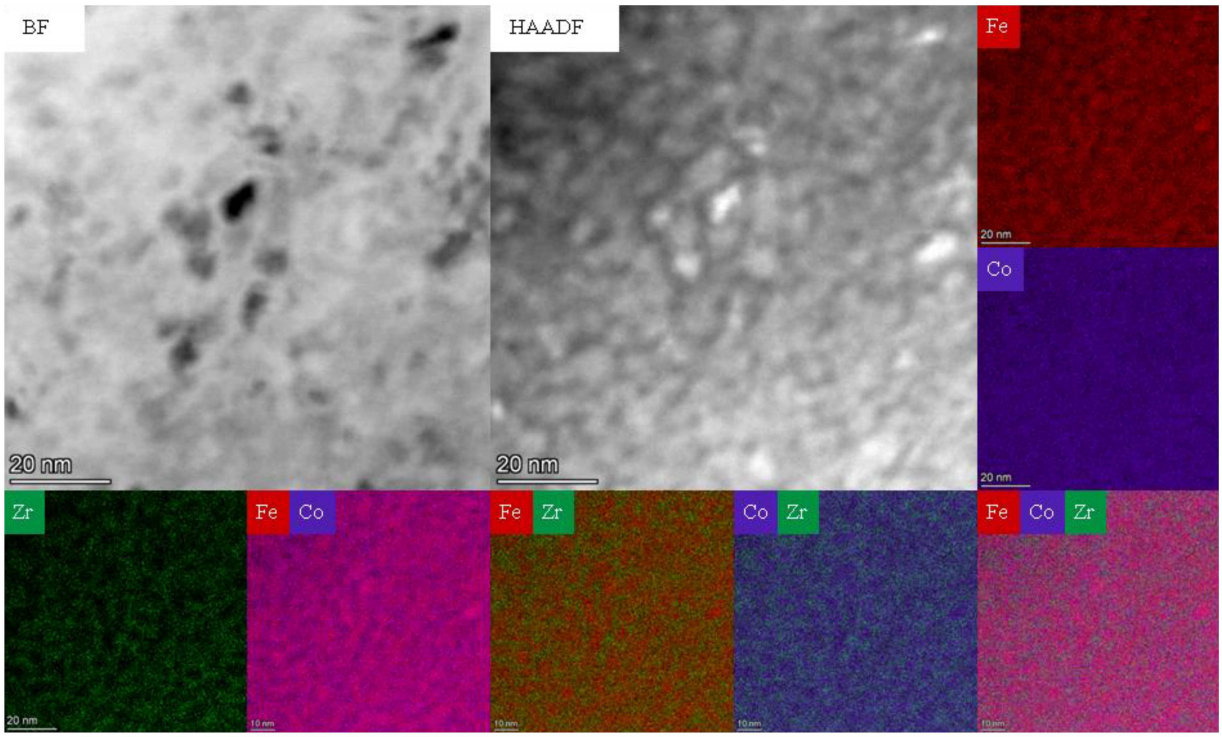

Fig. 4. BF-TEM and HAADF images with corresponding EDS maps of the alloy annealed at 550°C. In the EDS maps for FeCo and FeCoZr, the effect of Fe and Co overlapping when the maps are stacked together appears as pink areas.

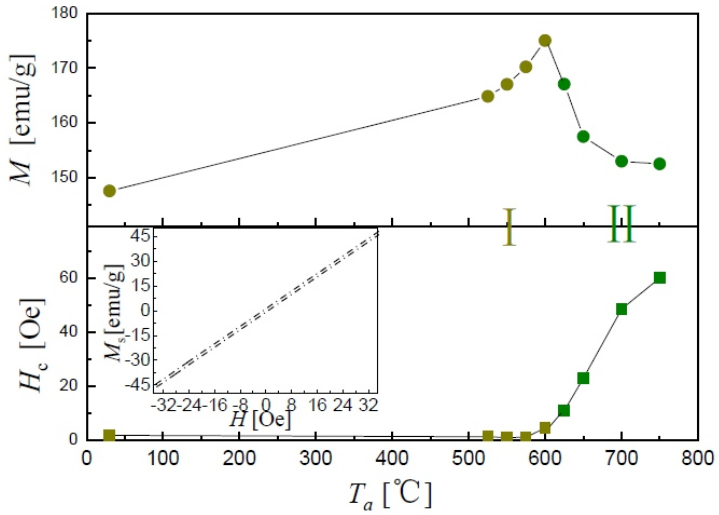

Fig. 5. The results of H_c and M_s of $Fe_{42}Co_{42}Zr_7B_9$ alloy as a function of annealing temperature. Inset shows the magnified low-field region of the hysteresis loop of the alloy sample annealed at 550°C.

treatment, which alleviated the internal stress induced by rapid solidification. The second stage corresponds to the two-phase structure comprising α-Fe(Co) nanocrystals embedded in an amorphous matrix. At 550°C, the magnified hysteresis loop exhibited an extremely low value of H_c . According to the random anisotropy model, excellent soft magnetic properties are obtained when fine ferromagnetic nanocrystals are exchange-coupled through the amorphous matrix at $D < L_{ex}$, where L_{ex} is the exchange correlation length ($L_{ex} \approx$ 20–40 nm for Fe-based alloys [16]). The saturation magnetization M_s increased with annealing temperature in the first stage due to the formation of bcc α-Fe(Co) crystals. In the second stage (above 600°C), H_c increased rapidly, most likely because of excessive grain growth and phase transformations. In contrast, M_s decreased with further

increase in annealing temperature due to precipitation of compounds such as $ZrCo_3B_2$ and Fe_3Zr. The resulting high H_c and low M_s values indicate degradation of the soft magnetic properties. Therefore, high-temperature annealing was observed to be detrimental to the soft magnetic properties of the alloy.

4. Conclusions

The crystallization behavior and magnetic property of the $Fe_{42}Co_{42}Zr_7B_9$ alloy during annealing were studied in a comprehensive way using DSC, XRD, TEM, and PPMS.

- The DSC curve of the as-quenched alloy revealed two exothermic peaks corresponding to (i) the primary crystallization of the α-Fe solid solution and (ii) the formation of $ZrCo_3B_2$ and Fe_3Zr phases.
- The growth of grain size was gradual in the early stage of crystallization and rapidly accelerated in the later stage. The lattice constant initially increased, reaching a maximum at 600°C due to the incorporation of Zr into the α-Fe lattice, and then decreased with further annealing.
- TEM analysis showed that the alloy annealed at 550°C is a two-phase structure comprising α-Fe(Co) nanocrystals embedded within an amorphous matrix.
- Both the specific saturation magnetization M_s and the coercivity H_c followed a two-stage trend. The M_s values first increased and then decreased, whereas the H_c values slightly increased below 600°C and then increased sharply due to grain growth and phase transformations.
- The alloy annealed in the early stage of crystallization, characterized by low H_c and high M_s values, exhibits excellent soft magnetic performance. It has potential applicability in miniaturized and lightweight electromagnetic components.

Acknowledgments

This work was supported by the National Natural Science Foundation of China (Grant No. 22279014), the Natural Science Foundation of Jilin Province (Grant No. YDZJ202201ZYTS319), and the Program for Science and Technology of the Education Department of Jilin Province (Grant No. JJKH20240567KJ). The authors also thank Sinomate Institute of Materials Research (Guang Zhou) Co., Ltd (SIMR), for assisting with the TEM and SEM characterizations.

References

[1] G. Herzer, *Acta Mater.* **61**, 718 (2013).

[2] K. Suzuki, J.M. Cadogan, *Phys. Rev. B* **58**, 2730 (1998).

[3] M.A. Willard, M. Daniil, in: *Handbook of Magnetic Materials*, Vol. 21, Elsevier 2013, p. 173.

[4] A.I. Bazlov, D.A. Milkova, E.N. Zanaeva, I.V. Strochko, N.Y. Tabachkova, A. Inoue, *J. Alloys Compd.* **1006**, 176247 (2024).

[5] Y. Sun, Z. Wang, S.C. Xu, Z. Hua, *Chin. Phys. B* **30**, 038103 (2021).

[6] K. Kotynia, P. Pawlik, M. Hasiak, M. Pruba, K. Pawlik, *Acta Phys. Pol. A* **131**, 1204 (2017).

[7] X. Lin, W. Yang, H. Liu, H. Man, A. Wang, C. Chang, B. Shen, *J. Magn. Magn. Mater.* **419**, 198 (2016).

[8] J. Salach, R. Szewczyk, P.S. Svec et al., *Acta Phys. Pol. A* **127**, 617 (2015).

[9] X.S. Li, Z.Y. Xue, X.B. Hou, G.Q. Wang, X. Huang, H.B. Ke, B.A. Sun, W.H. Wang, *Intermetallics* **131**, 107087 (2021).

[10] M.A. Willard, D.E. Laughlin, M.E. McHenry, D. Thoma, K. Sickafus, J.O. Cross, V.G. Harris, *J. Appl. Phys.* **84**, 6773 (1998).

[11] J.Y. Huang, W. Zhang, W.P. Fang, Y. Yi, *Tribol. Int.* **185**, 108485 (2023).

[12] G. Rajesh, M.A. Rahman, S. Jeavudeen, *J. Phys. Conf. Ser.* **2925**, 012009 (2024).

[13] K.H. Kang, X. An, K. Chung, J.-W. Kim, *J. Alloys Compd.* **1032**, 181236 (2025).

[14] F. Chai, Z. Ma, X. Han, J. Feng, X. Hu, L. Hua, *J. Alloys Compd.* **1020**, 179410 (2025).

[15] C. Zheng, Q. Wang, R. Chen, W. Wei, Y. Su, H. Fu, *Int. J. Refract. Met. Hard Mater.* **131**, 107211 (2025).

[16] K. Suzuki, G. Herzer, J.M. Cadogan, *J. Magn. Magn. Mater.* **177–181**, 949 (1998).